ACS OMEGA

Open Access

http://pubs.acs.org/journal/acsodf

Article

Doping Strategy of Monolayer MoS_2 to Realize the Monitoring of Environmental Concentration of Desflurane: A First-Principles Study

Kaixin Wang,[⊥] Shiwen Fan,[⊥] Benli Liu, Weihao Liu, and Xiangdong Chen*

Cite This: *ACS Omega* 2024, 9, 36659−36670

Read Online

ACCESS | Metrics & More | Article Recommendations | Supporting Information

ABSTRACT: Desflurane is a new volatile inhalation anesthetic that is widely used in medical operation. However, various diseases can be caused by chronic exposure to desflurane, which is also a greenhouse gas. Therefore, it is urgent to find a suitable method for monitoring desflurane. In this paper, the process of doping of Pd, Pt, and Ni on the MoS_2 surface is simulated to determine the stability of the doping structure based on first-principles. The adsorption properties and sensing properties of Pd-MoS_2, Pt-MoS_2, and Ni-MoS_2 on desflurane are explored by parameters including independent gradient model based on Hirshfeld partition (IGMH), electron localization function (ELF), and density of states (DOS), sensibility, and recovery time, subsequently. The doping results show that the three doping systems (Pd-MoS_2, Pt-MoS_2, and Ni-MoS_2) are structurally stable, and the chemical bonds are formed with MoS_2. The adsorption results show the best chemisorption between Pt-MoS_2 and desflurane with the chemical bonds between them. The results of IGMH, ELF, and DOS also confirm it. The sensing characterization results show that the recovery time of Pt-MoS_2 ranges between 85.27 and 0.027 s, and the sensitivity ranges from 99.26 to 25.69%, all of which can meet the requirements of the sensor. Considering the adsorption effect and sensing characteristics, Pt-MoS_2 can be used as a gas-sensitive material for detecting the concentration of desflurane.

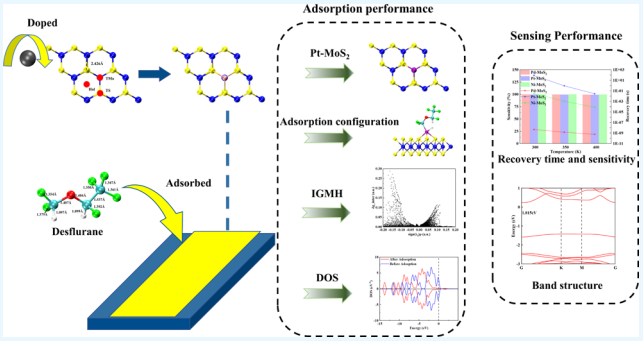

1. INTRODUCTION

Desflurane ($C_3H_2OF_6$) is a new volatile halogenated inhalation anesthetic.[1−5] The blood solubility and lesser circulation uptake of $C_3H_2OF_6$ is less compared to other anesthetics.[6,7] In addition, $C_3H_2OF_6$ has a lower tissue solubility, and small amounts of $C_3H_2OF_6$ in tissues are rapidly eliminated through lungs at the end of operation even with prolonged general anesthesia.[8−10] As a result, $C_3H_2OF_6$ has been widely used in clinical procedures.[11]

The invention of anesthesia drugs[12] including $C_3H_2OF_6$ greatly contributed to the advancement of modern medicine. However, serious leakage contamination of $C_3H_2OF_6$ in the operating room occurred due to imperfections in the administration route and anesthetic delivery system. The U.S. Occupational Safety and Health Administration (OSHA) estimates that more than 250,000 healthcare workers may be exposed to $C_3H_2OF_6$ and are at risk for related diseases.[13] The time that $C_3H_2OF_6$ concentrations exceeded the National Institute of Occupational Safety and Health (NIOSH) standards was up to 50% during operation.[14] It has been reported that prolonged exposure to $C_3H_2OF_6$ may lead to adverse effects including cognitive disorder and neurodegenerative disorders.[15,16] In addition, $C_3H_2OF_6$ is a synthetic chemical, and its impact on the atmospheric environment is a growing public concern. The global warming potential (GWP) of $C_3H_2OF_6$ is 2540 times greater than that of CO_2, and it takes up to 14 years to decompose in nature.[17−19] Considering the occupational exposure risk and the environmental hazards of $C_3H_2OF_6$, there is a strong need to monitor exposure to $C_3H_2OF_6$.

Electrochemical sensors are used in gas detection with low energy consumption, small size, and high sensitivity.[20−22] The electrochemical sensor is a device that uses a semiconductor gas-sensitive material as the main sensing component. The composition and concentration are analyzed by measuring the trend and magnitude of the conductivity change of the gas-sensitive material before and after exposing to the gas.[23,24] Transition metal dichalcogenides (TMDs) have been widely studied as gas-sensitive materials for electrochemical sensors.[25] In fact, TMDs have long been used in the medical field.[26] Lakshmy et al. studied the application of Pd-doped $MoTe_2$ in glucose (GLU) detection, and the results showed that Pd-$MoTe_2$ can be used as a candidate material for GLU detection.[27] Wan et al. found that Ru-$MoTe_2$ exhibits strong adsorption properties for volatile organic compounds (VOC) markers and can be used for early diagnosis of lung cancer.[28] Sadeghi et al.

Received: June 1, 2024
Revised: July 28, 2024
Accepted: August 5, 2024
Published: August 15, 2024

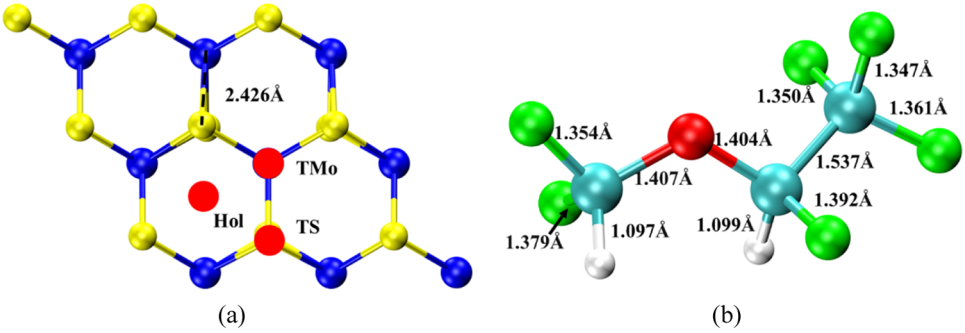

Figure 1. Molecular structure of (a) MoS_2 and (b) $C_3H_2OF_6$.

investigated the detection effect of monolayer MoS_2 on DNA. The results showed that MoS_2 can also be used in medical detection of nucleic acid sequences.[29] TMDs are considered to be used in the detection of desflurane due to their wide application in the medical field. Among TMDs, MoS_2 is a semiconductor with large work function, high electron affinity, and reasonable carrier mobility, which lead to a great application potential in the gas sensors field.[30,31] It has been shown that the electronic properties can be tuned to enhance the adsorption and sensing properties of MoS_2 on gas molecules by doping metal on MoS_2.[32] Therefore, the modification of MoS_2 by doping several metal atoms will achieve low energy consumption, small size, and high sensitivity of $C_3H_2OF_6$ concentration monitoring equipment. It is of great engineering significance to reduce the risk of occupational exposure and environmental hazards of $C_3H_2OF_6$.

Above, in this paper, the process of doping of Pd, Pt, and Ni on the MoS_2 surface is simulated to determine the rationality of the doping structure based on the first-principles. The adsorption properties of Pd- MoS_2, Pt- MoS_2, and Ni-MoS_2 on $C_3H_2OF_6$ were investigated by calculating the parameters of independent gradient model based on Hirshfeld partition (IGMH), electron localization function (ELF), and density of states (DOS). The sensing characteristics of the three gas-sensitive materials for the detection of determination are comprehensively evaluated in combination with sensitivity and recovery properties. Finally, the potential applications of the three materials in $C_3H_2OF_6$ detection are evaluated by combined adsorption properties and sensing characteristics.

2. COMPUTATION DETAILS

In this paper, a $4 \times 4 \times 1$ MoS_2 cell structure containing 9 Mo atoms and 18 S atoms is built based on Material Studio, and the vacuum thickness is set to 15 Å. The Visual Molecular Dynamics (VMD) is used for visualization. As shown in Figure 1a, the Mo−S−Mo bond angle and Mo−S bond length are 81.52° and 2.426 Å, which is in general agreement with the literature,[33,34] indicating that the parameters and methods used in this paper are reliable. The bond lengths of $C_3H_2OF_6$ are shown in Figure 1b. The geometric optimizations in this paper are done with the quickstep package in cp2k by Broyden−Fletcher−Goldfarb−Shanno (BFGS).[35] The Goedecker-Teter-Hutter (GTH)-PBE is used as pseudopotential and DZVP-MOLOPT-SR-GTH as basis set. Considering both accuracy and computational cost, this study uses DFT-D3(BJ) for dispersion correction.[36−38] The cutoff and real cutoff are set as 800 and 50 Ry, respectively. The k point is set to $5 \times 5 \times 1$. And all calculations are considered spin-polarized. The Brillouin zone meshing convergence and energy cutoff convergence tests are shown in Tables S1 and S2.

The binding energy E_{bind} of metal atoms (Pd, Pt, and Ni) on the MoS_2 surface and the adsorption energy E_{ad} of $C_3H_2OF_6$ on the monolayer surface are calculated as follows:

$$E_{bind} = E_{metal-MoS_2} - E_{metal} - E_{MoS_2} \quad (1)$$

$$E_{ad} = E_{gas/layer} - E_{gas} - E_{metal-MoS_2} \quad (2)$$

where $E_{metal-MoS_2}$, E_{metal}, E_{MoS_2}, $E_{gas/layer}$, and E_{gas} denote the total energy of metal-doped MoS_2, metal atom, MoS_2 molecular layers, adsorption system, and gas, respectively.

The charge transfer in this paper is calculated by the Hirshfeld method as below:

$$Q_T = -\int \frac{\rho_A^0(r)}{\sum_A \rho_A^0(r)} \left[\rho(r) - \sum_A \rho_A^0(r)\right] dr \quad (3)$$

where $\rho_A^0(r)$ and $\rho(r)$ are the charge density of individual atoms and whole system, respectively. When $Q_T > 0$, the system loses charges and the system gains charges, conversely.

The charge transfer during adsorption is further analyzed by calculating the charge density difference (CDD) $\Delta\rho$ as follows:

$$\Delta\rho = \rho_{gas/monolayer} - \rho_{monolayer} - \rho_{gas} \quad (4)$$

where ρ_{gas}, $\rho_{gas/monolayer}$, and $\rho_{monolayer}$ denote the charge density of the gas and the adsorption system after and before adsorption, respectively.

In this article, IGMH is used to analyze the intermolecular forces. The type and strength of intermolecular forces are analyzed by sign$(\lambda_2)\rho$ function.[39,40] When sign$(\lambda_2)\rho < 0$, the intermolecular force is attraction, and repulsion conversely. When sign$(\lambda_2)\rho \approx 0$, the intermolecular force is van der Waals forces. ELF is a spatial function used to study the electronic structure of a system for describing the bonding of atoms. It can reflect the situation of charge transfer in the corresponding area. When the charge transfer is strong, the ELF of the area will also increase. The closer ELF is to 1, the higher the adsorption capability.[41,42] Both IGMH and ELF are calculated using Multiwfn.[43] The DOS is a function of the electron energy. PDOS can be used to evaluate whether the atoms are bonded. If the PDOS of two atoms overlap, this is due to the atoms sharing electrons, and it also indicates that there is an interaction between the two atoms.

The sensing characteristics of electrochemical sensors mainly include recovery time τ. The expression of sensitivity S is shown below:

$$\sigma = Ae^{-B_g/2kT} \quad (5)$$

https://doi.org/10.1021/acsomega.4c05159
ACS Omega 2024, 9, 36659−36670

Table 1. Doped Energy and Charge Transfer in Each Doped System

doped system	doped site	E_{bind} (eV)	ΔQ (e)
Pd	TS	−1.987	0.104
	TMo	−2.593	0.153
	Hol	−2.239	0.123
Pt	TS	−3.252	−0.005
	TMo	−3.841	0.130
	Hol	−3.226	0.097
Ni	TS	−2.772	−0.065
	TMo	−4.559	−0.142
	Hol	−4.103	−0.112

$$S = \left| \frac{\frac{1}{\sigma_{after}} - \frac{1}{\sigma_{before}}}{\frac{1}{\sigma_{before}}} \right| \quad (6)$$

where A is a constant, k is the Boltzmann constant, T is the temperature, and σ_{before} and σ_{after} denote the conductivity before and after adsorption of the gas, respectively.

The defining equation for the recovery time of the sensor is shown below:

$$\tau = A^{-1} e^{-E_g/kT} \quad (7)$$

where A is the attempt frequency with a value of 10^{12} s^{-1} and E_g is the potential barrier with a value consistent with E_{ad}.

To further analyze the adsorption behavior of gas on metal-doped MoS_2, the work function φ of all adsorption systems is analyzed. It can be given by the following equation:[44]

$$\varphi = E_V + E_F \quad (8)$$

where E_V and E_F denote the vacuum level and Fermi level, respectively.

3. RESULT AND DISCUSSION

3.1. Metal−MoS_2 Monolayer Analysis. *3.1.1. Doping Configuration Analysis.* As shown in Figure 1a, there are three sites for metal doping on MoS_2, including TMo (above the Mo atoms), TS (above the S atoms), and Hol (above the holes) according to the structural characteristics of MoS_2.

The binding energy and charge transfer for each doping system are shown in Table 1. It can be seen that the doping system is the most stable structure when the metal atom is located in TMo with the largest binding energy and charge transfer.

The phonon band structure of each system is calculated by phonopy to evaluate the stability of each structure.[45] The phonon spectra along the high-symmetry path (M → G → K) of the Brillouin zone are shown in Figure 2. It can be seen that no imaginary phonon frequency is shown in the whole Brillouin zone, indicating that these systems are dynamically stable.

As shown in Figure 3, the large binding energy and electron transfer suggest the formation of Pd−S, Pd−S, and Ni−S bonds. In both the Pd-MoS_2 and Pt-MoS_2 systems, the Pd and Pt atoms

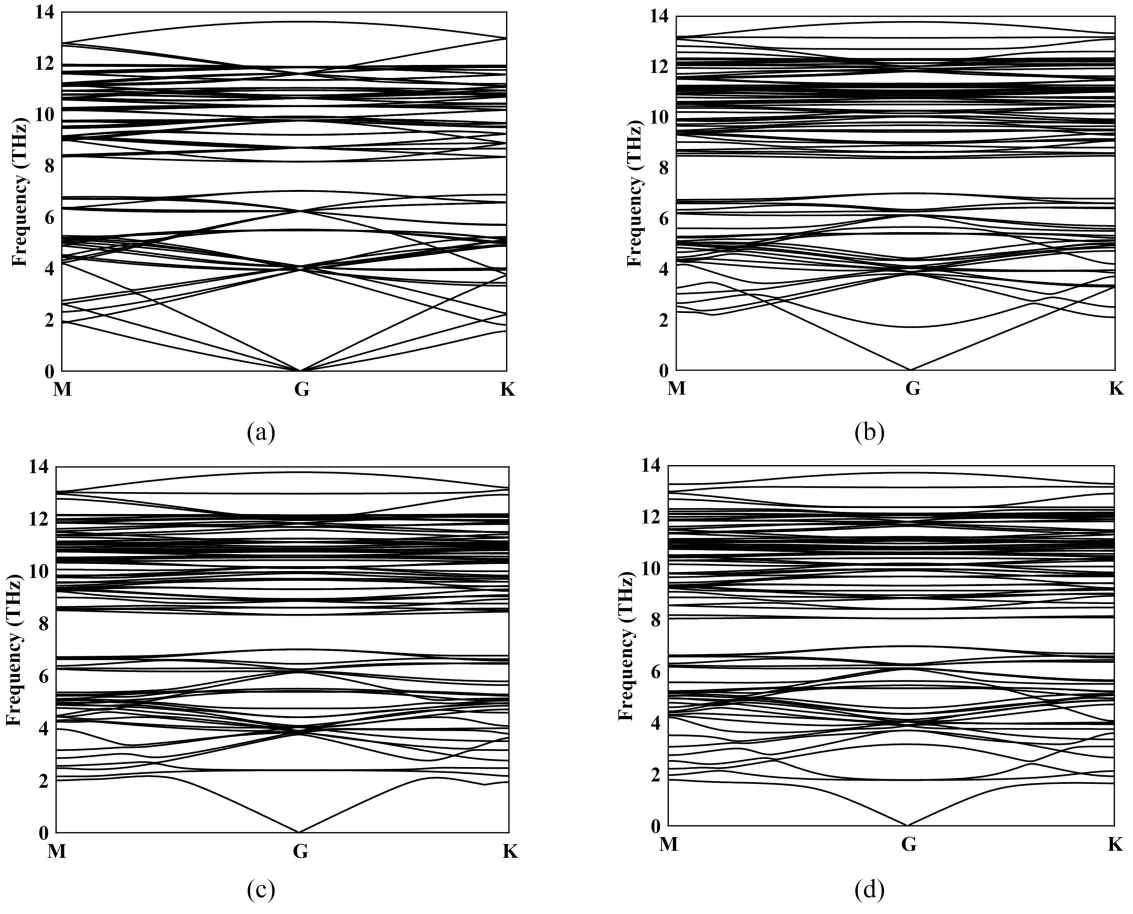

Figure 2. Phonon band structure of (a) MoS_2, (b) Ni-MoS_2, (c) Pt-MoS_2, and (d) Pd-MoS_2.

https://doi.org/10.1021/acsomega.4c05159
ACS Omega 2024, 9, 36659−36670

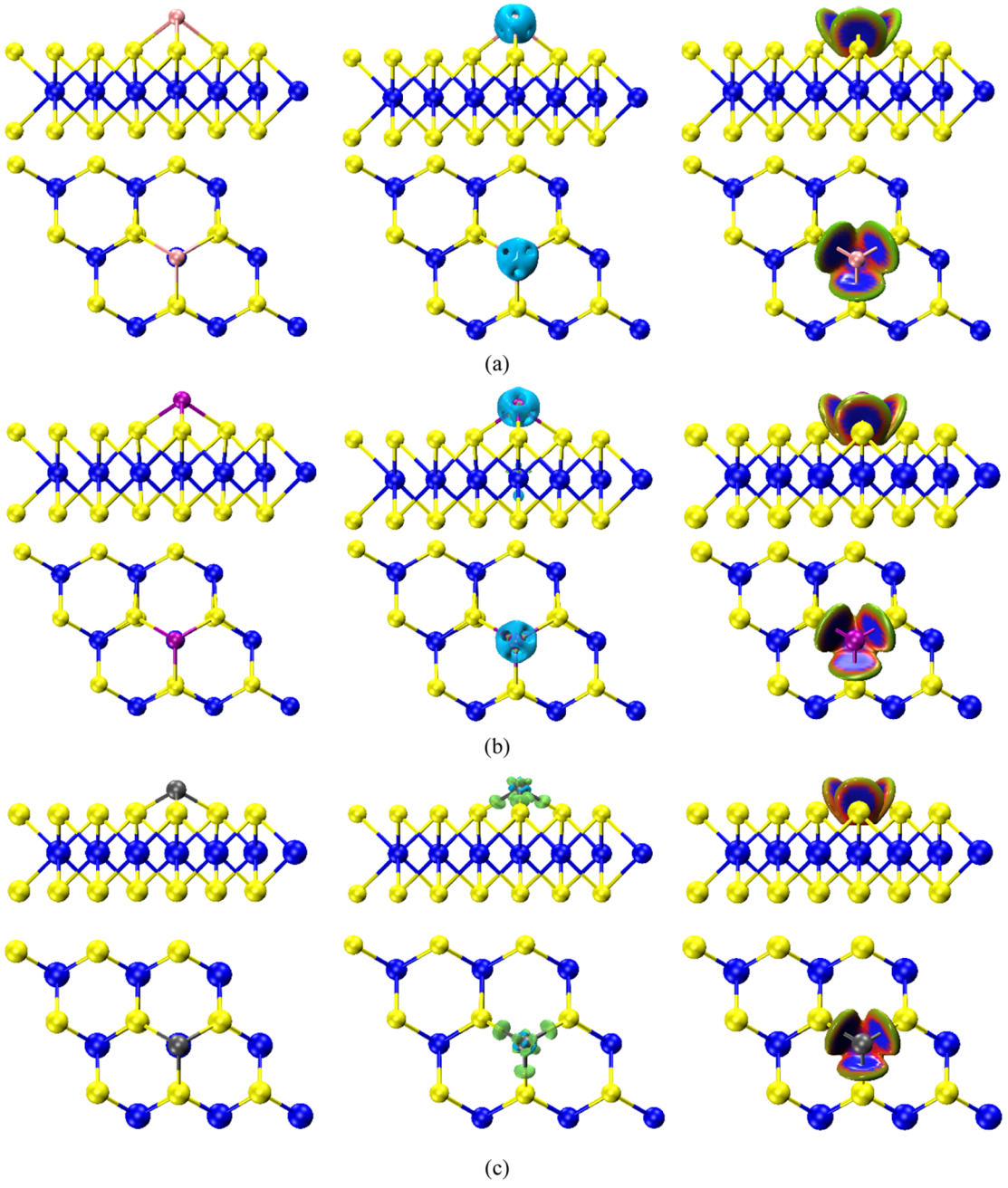

Figure 3. Most stable configuration and results of CDD and IGMH in (a) Pd-MoS_2, (b) Pt-MoS_2, and (c) Ni-MoS_2. The CDD and IGMH isovalues of $C_3H_2OF_6$/Pd-MoS_2, $C_3H_2OF_6$/Pt-MoS_2, and $C_3H_2OF_6$/Ni-MoS_2 is 0.01 au. Green is for electron dissipation regions, and blue is for electron accumulation regions in CDD. Blue is for attraction, and green is for repulsion in IGMH.

are surrounded by blue regions, indicating that Pd and Pt lose charges to the S atoms during the doping process. In contrast, the Ni atom and Ni−S bonds are surrounded by a green region, indicating that Ni gains charges in the doping process, which is consistent with the analysis of charge transfer. The results of IGMH analysis show a blue attraction interaction region between Pd, Pt, Ni, and S atoms, which originates from the chemical bond formed between dopant atoms and S atoms. This corresponds to the peak near $\text{sign}(\lambda_2)\rho = -0.1$ au in Figure 4. Additionally, there is a red repulsion region in the middle of the blue attraction region, which may be due to the ring potential resistance effect from bonding between atoms, corresponding to the peak near $\text{sign}(\lambda_2)\rho = 0.05$ au in Figure 4.[46] In general, the attraction interaction is stronger than the repulsion interaction, and Pd, Pt, and Ni can be stably doped on the surface of MoS_2.

The charge density in each doped system is shown in Figure 5. It can be seen that the charge density of the system remains relatively stable in the range of 0−3 Å, but it changes significantly in the range of 3−6 Å. This phenomenon is attributed to the formation of stable chemical bonds between the doping atoms and the substrate, leading to the localization of numerous electrons in this region. The influence of doping atoms on the electronic structure of MoS_2 surface is significant. The electron density near the doped atoms increases significantly, showing a certain degree of ionicity.[47] This alteration enhances the gas adsorption capacity.[48]

https://doi.org/10.1021/acsomega.4c05159
ACS Omega 2024, 9, 36659−36670

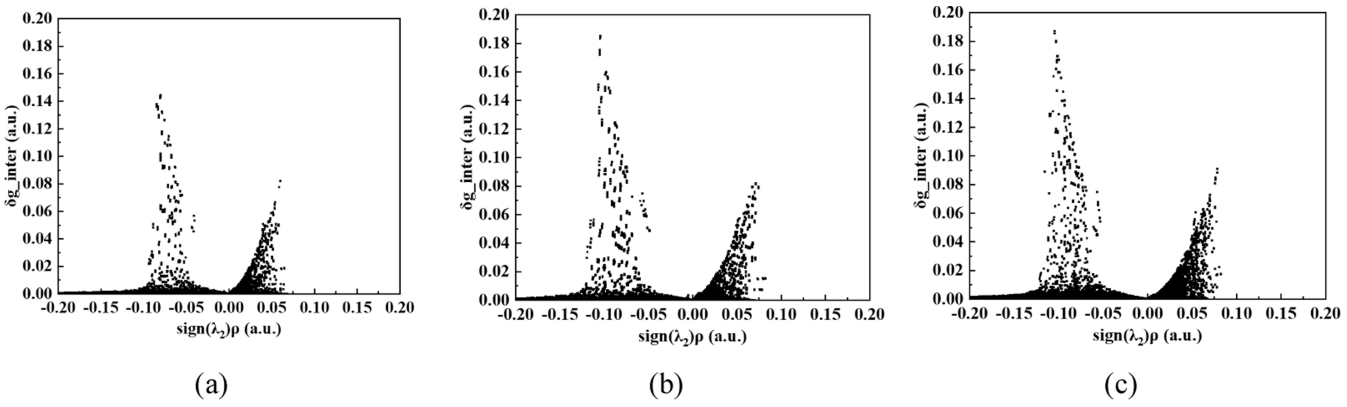

Figure 4. Scatter plot of IGMH in (a) Pd-MoS_2, (b) Pt-MoS_2, and (c) Ni-MoS_2.

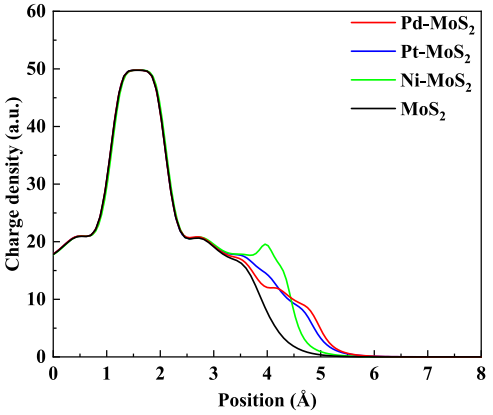

Figure 5. Charge density along the Z axis in each system.

The energy changes of the adsorption process of each system are shown in Figure 6. It can be seen that the energy barriers of each system during the adsorption process are 0.741, 0.873, and 0.026 eV, respectively. The energy barrier of Ni-MoS_2/$C_3H_2OF_6$ is close to 0 because its initial adsorption configuration resembles the most stable configuration. The energy barriers of each system are below the critical barrier (0.91 eV), indicating a smooth adsorption process.[49]

3.1.2. DOS Analysis in Doping Process. DOS is a function of energy as a variable to evaluate intermolecular interactions. As shown in Figure 7, the total DOS of Pd-MoS_2, Pt-MoS_2, and Ni-MoS_2 is overall shifted to lower energies after being doped with metal atoms. This indicates that the systems tend to be more stable after doping with metal atom doping. In the Pd-MoS_2 system, there is no significant change in the structure of the underlying MoS_2, with no significant change in DOS. The substantial overlap between the Pd 4d orbital, S 3p orbital, and Mo 4d orbitals in the ranges of −7 to 0.5 eV and 1.5−5 eV suggests the hybridization among these orbitals, promoting the formation of Pd−S bonds. Similarly, in Pt-MoS_2, there is no significant change in MoS_2 after Pt doping. The orbital hybridization among the Pt 5d orbital, S 3p orbital, and Mo 4d orbital also contributes to bond formation. The DOS of Ni-MoS_2 at the Fermi level is changed by Ni doping, leading to a change in conductivity. The PDOS result indicates the formation of a chemical bond between Ni and Mo. Furthermore, the symmetric DOS also indicates that metal−MoS_2 does not exhibit magnetism during the doping process.

3.2. Adsorption Property Analysis. *3.2.1. Adsorption Configuration Analysis.* In this article, the most stable adsorption configurations of Pd-MoS_2, Pt-MoS_2, and Ni-MoS_2 with $C_3H_2OF_6$ are analyzed. The adsorption energy and charge transfer in each system are shown in Table 2.

The adsorption configuration of Pd-MoS_2 on $C_3H_2OF_6$ is shown in Figure 5a. There is no stable chemical bond formation due to the weak adsorption energy and charge transfer between Pd-MoS_2 and $C_3H_2OF_6$. The IGMH results show that only a few green areas exist between $C_3H_2OF_6$ and Pd-MoS_2, which exhibit weak van der Waals forces. This corresponds to the peak at $\text{sign}(\lambda_2)\rho \approx 0$ in Figure 8a. The adsorption energy and charge transfer of Pt-MoS_2 with $C_3H_2OF_6$ are the largest, reaching −0.834 eV and −0.235e. The large adsorption energy allows bonding between C3H2OF6 and Pt-MoS_2, and the Pt−H and

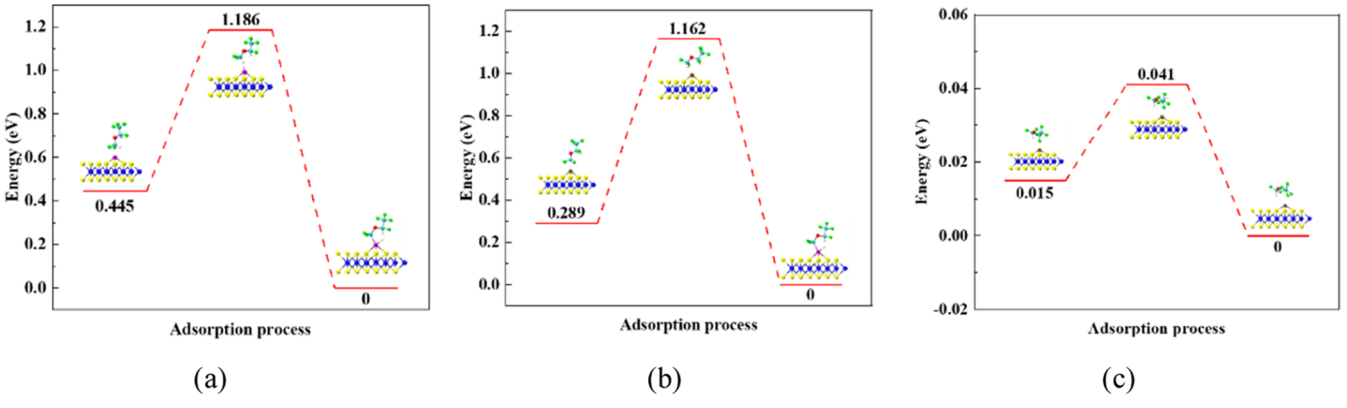

Figure 6. Energy change during the adsorption process in (a) Pd-MoS_2, (b) Pt-MoS_2, and (c) Ni-MoS_2.

https://doi.org/10.1021/acsomega.4c05159
ACS Omega 2024, 9, 36659−36670

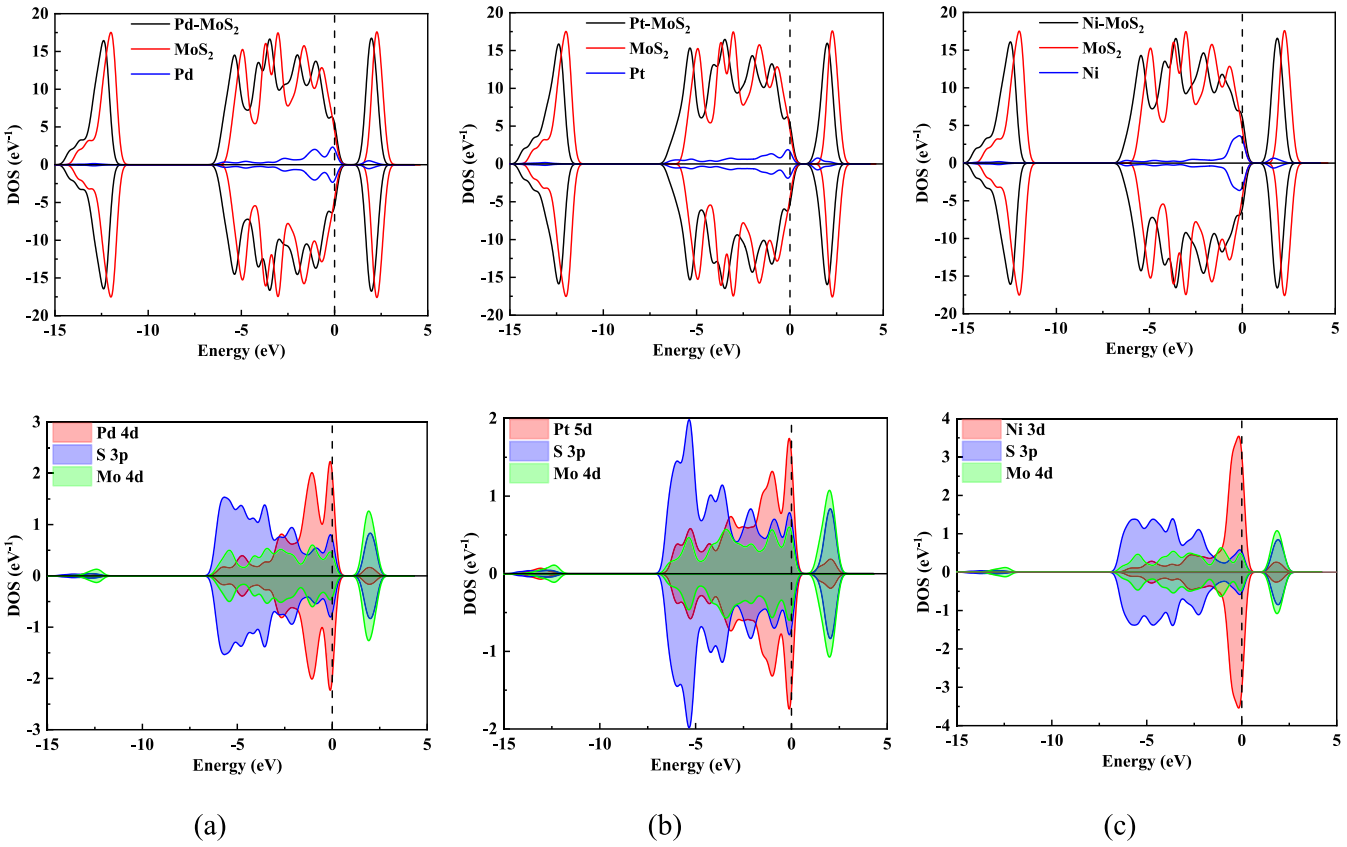

Figure 7. DOS and PDOS of (a) Pd-MoS_2, (b) Pt-MoS_2, and (c) Ni-MoS_2.

Table 2. Adsorption Energy and Charge Transfer in Each Adsorption Systems

adsorption system	adsorption energy (eV)	charge transfer (e)	adsorption distance (Å)
Pd-MoS_2/$C_3H_2OF_6$	−0.219	−0.064	Pd−H: 3.689 Pd−F: 2.806
Pt-MoS_2/$C_3H_2OF_6$	−0.834	−0.235	Pt−H: 1.567 Pt−C: 2.033
Ni-MoS_2/$C_3H_2OF_6$	−0.629	−0.103	Ni−F: 2.109

Pt−C bonds are 1.567 and 2.033 Å, respectively. In addition, the extremely strong adsorption energy causes the break of the C−H bond. In the result of CDD, the C, H, and F atoms are surrounded by electron-concentrating regions which act as electron acceptors. This is consistent with the previous analysis. The IGMH results indicate the formation of strong attraction between $C_3H_2OF_6$ and Pt-MoS_2 (blue region) which corresponds to the peak at sign$(\lambda_2)\rho = -0.15$ au Additionally, there is a small number of red regions around the blue region which is the repulsion generated by the ring steric effect related to the peak at sign$(\lambda_2)\rho$ = 0.1 au Overall, the attraction effect of Pt-MoS_2 to $C_3H_2OF_6$ is stronger than the effect of repulsion. The adsorption configuration of $C_3H_2OF_6$/Ni-MoS_2 is shown in Figure 8c. There is no chemical bond forming between Ni-MoS_2 and $C_3H_2OF_6$, which is corroborated by weak adsorption energy and charge transfer. The IGMH results show that there are only a few blue attraction regions between $C_3H_2OF_6$ and Ni-MoS_2, which are slightly stronger than the van der Waals force. However, the adsorption is physisorption without chemical bond forming (Figure 9).

3.2.2. DOS Analysis in Adsorption Process. In this paper, the DOS and PDOS of the adsorption system are shown in Figure 10. As shown in Figure 10a, the DOS of Pd-MoS_2 shifted to a lower level after adsorbing $C_3H_2OF_6$, and a new peak appears near −10 eV. It can be found that the DOS of $C_3H_2OF_6$ is basically unchanged after adsorption, indicating that the structure of $C_3H_2OF_6$ remains stable during the adsorption process. There is only a slight overlap between the H 1s orbital and Pd 4d orbital in the −5 to −2.5 eV range, resulting in weak hybridization that makes it difficult to form chemical bonds. In the Pt-MoS_2/$C_3H_2OF_6$ system, there is a significant change in the DOS near the Fermi energy level after adsorbing $C_3H_2OF_6$, leading to further alteration of the band gap. The DOS of $C_3H_2OF_6$ exhibits a minor peak in the −2.5 to 2.5 eV range postadsorption, indicating a significant structural change induced by the adsorption of Pt-MoS_2. The PDOS reveals a significant overlap of the Pt 5d orbital with H 1s and C 2p orbitals in the −10 to 0 eV range, suggesting strong hybridizations among Pt 5d, H 1s, and C 2p orbitals. These hybridizations facilitate bonding of Pt with H and C, aligning with earlier analysis.

As shown in Figure 10c, the structure of $C_3H_2OF_6$ is changed by Ni-MoS2, resulting in a notable decrease in its DOS peaks at −1.5 and −3 eV. The Ni 3d orbital and the F 2p orbital exhibit limited overlap between −7.5 and 2.5 eV, indicating insufficient hybridization to form a new C−Ni chemical bond.

3.2.3. ELF Analysis. To further explore the interactions in each adsorption system, the ELF is analyzed in this section. As shown in Figure 11, the degree of electronic localization between Pd-MoS_2 and $C_3H_2OF_6$ is close to 0 without a chemical bonding connection. The ELF value between C, H, and Pt atoms is close to 0.5, indicating electronic localization between Pt and

https://doi.org/10.1021/acsomega.4c05159
ACS Omega 2024, 9, 36659−36670

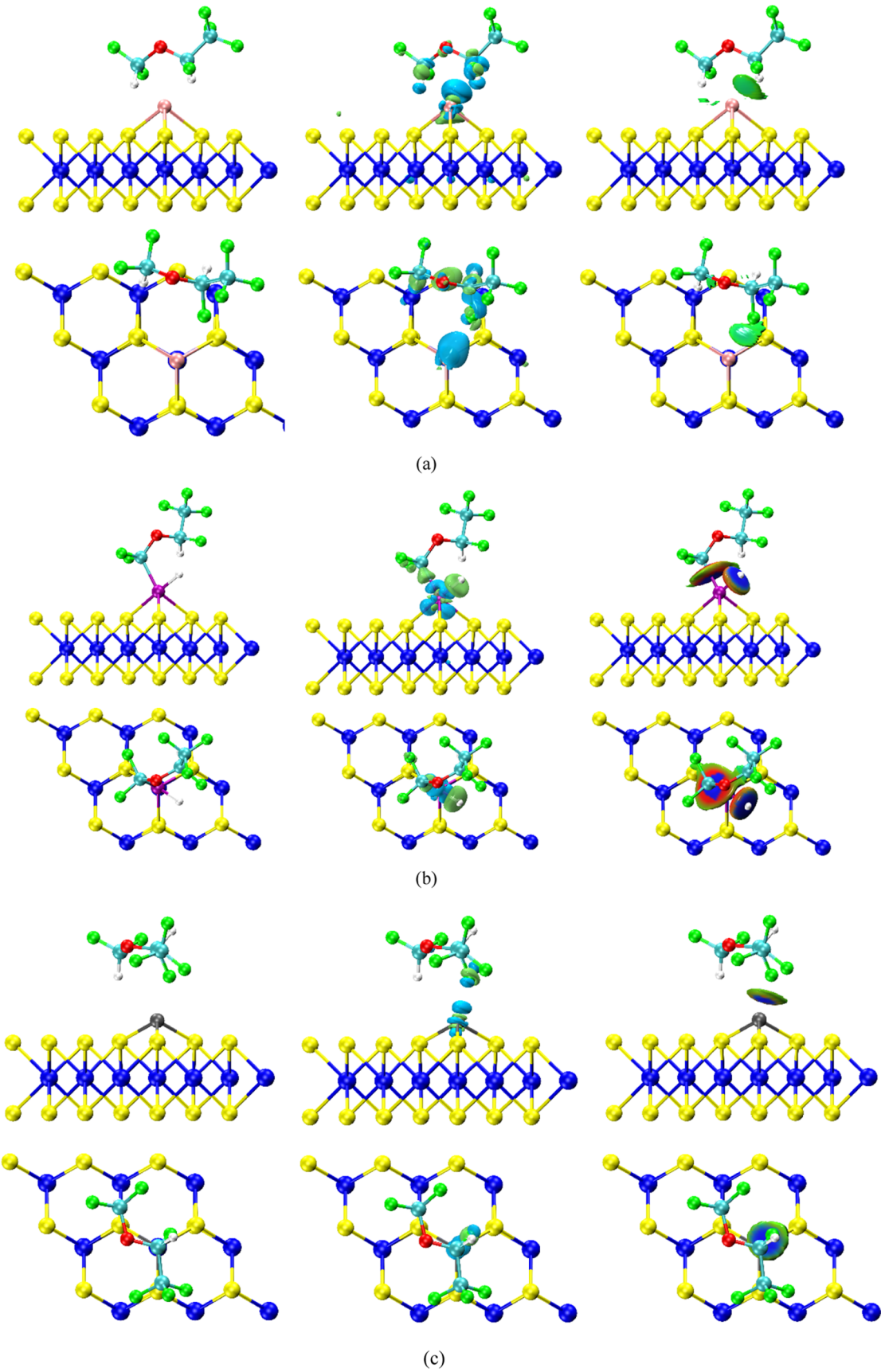

Figure 8. Most stable adsorption configuration and results of CDD and IGMH in (a) $C_3H_2OF_6$/Pd-MoS_2, (b) $C_3H_2OF_6$/Pt-MoS_2, and (c) $C_3H_2OF_6$/Ni-MoS_2. The CDD isovalues of $C_3H_2OF_6$/Pd-MoS_2, $C_3H_2OF_6$/Pt-MoS_2, and $C_3H_2OF_6$/Ni-MoS_2 are 0.01, 0.01, and 0.001 au, respectively. The IGMH isovalue of $C_3H_2OF_6$/Pd-MoS_2, $C_3H_2OF_6$/Pt-MoS_2, and $C_3H_2OF_6$/Ni-MoS_2 is 0.01 au.

https://doi.org/10.1021/acsomega.4c05159
ACS Omega 2024, 9, 36659−36670

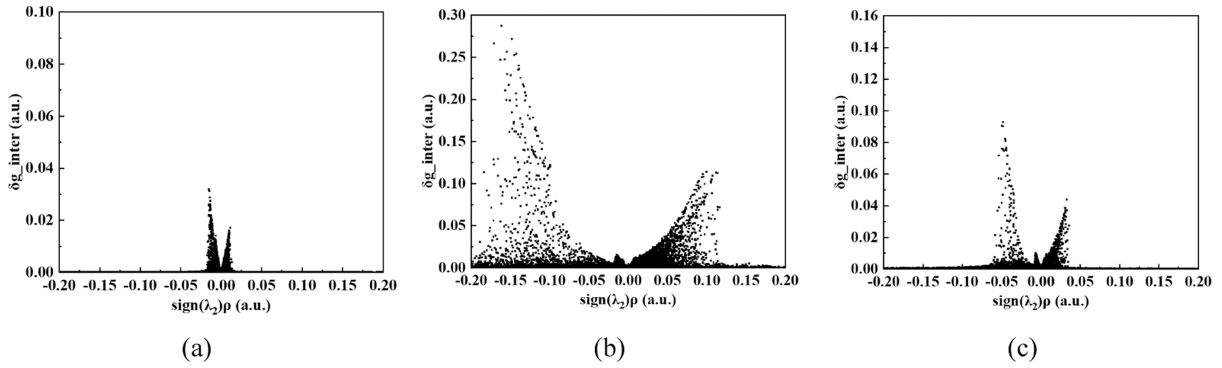

Figure 9. Scatter plot of IGMH in (a) $C_3H_2OF_6$/Pd-MoS_2, (b) $C_3H_2OF_6$/Pt-MoS_2, and (c) $C_3H_2OF_6$/Ni-MoS_2.

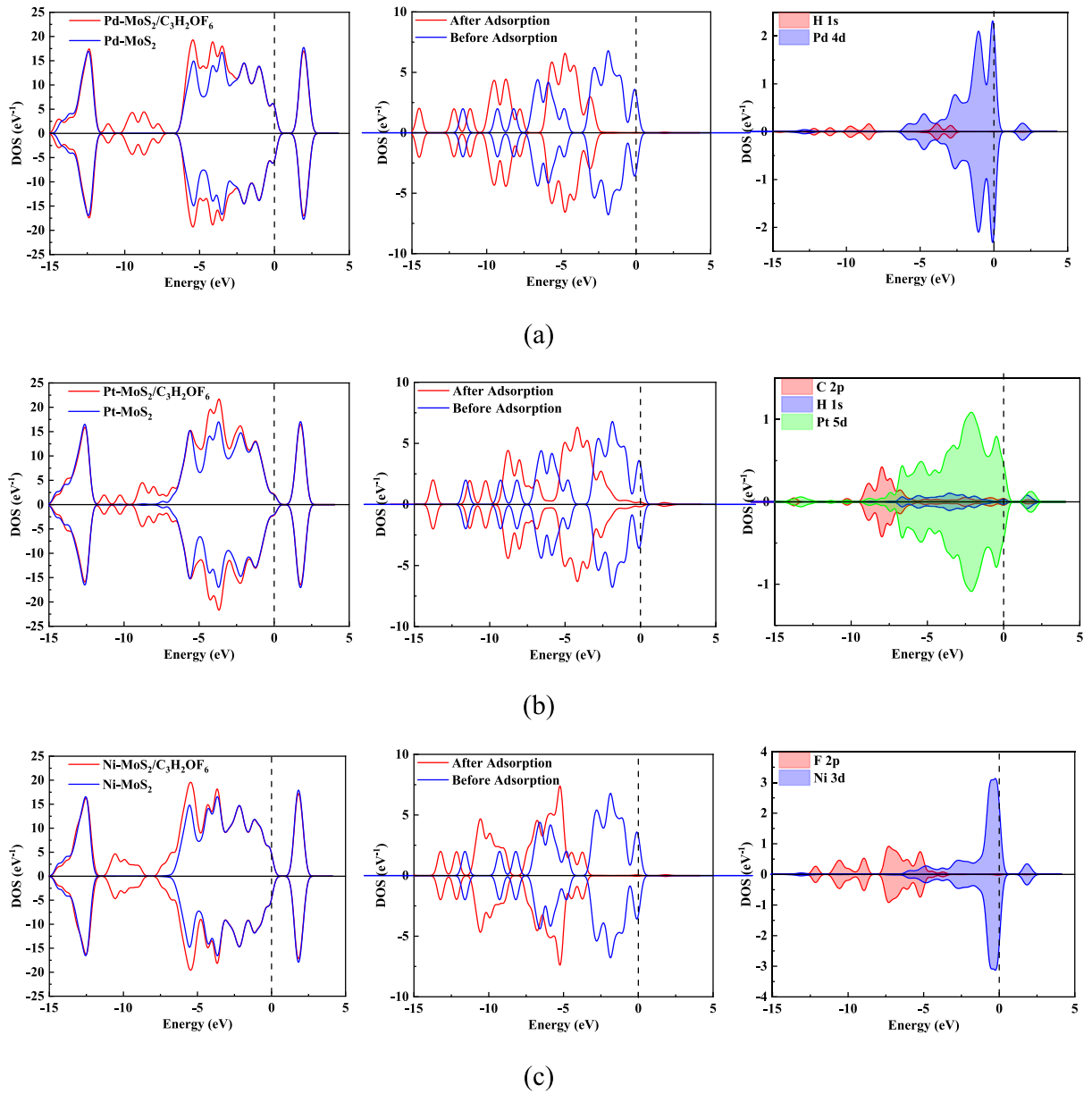

Figure 10. DOS and PDOS of (a) $C_3H_2OF_6$/Pd-MoS_2, (b) $C_3H_2OF_6$/Pt-MoS_2, and (c) $C_3H_2OF_6$/Ni-MoS_2.

C and H atoms with a clear bonding tendency. Similar to the Pd-MoS_2/$C_3H_2OF_6$ system, there is no chemical bonding connection between Ni and F atoms.

3.2.4. Work Function Analysis. The work functions for each adsorption system are listed in Figure 12. The work functions of all systems changed to varying degrees, and this change is correlated with the adsorption effect, indicating that a

https://doi.org/10.1021/acsomega.4c05159
ACS Omega 2024, 9, 36659−36670

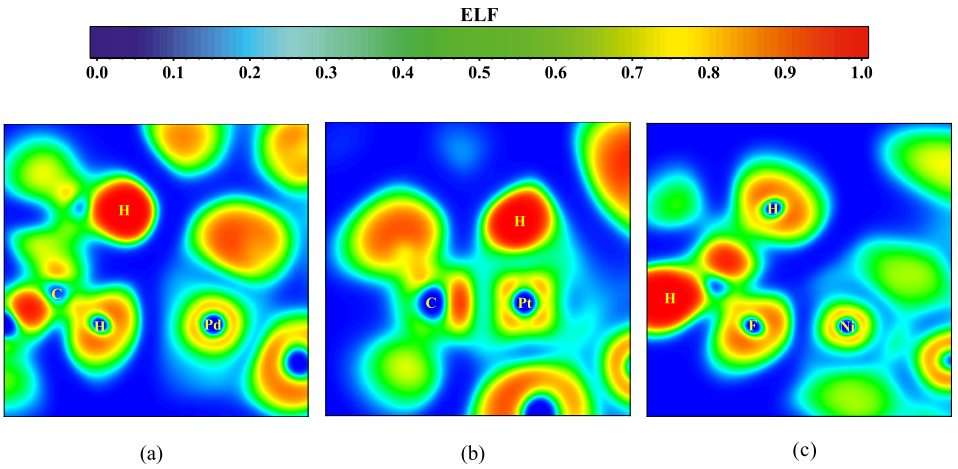

Figure 11. ELF of (a) $C_3H_2OF_6$/Pd-MoS_2, (b) $C_3H_2OF_6$/Pt-MoS_2, and (c) $C_3H_2OF_6$/Ni-MoS_2.

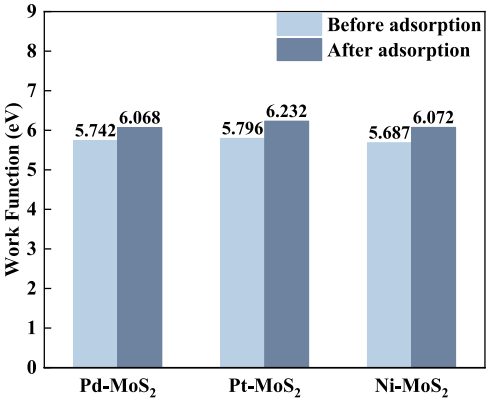

Figure 12. Work functions of each adsorption system.

reasonable interaction occurred between the adsorption substrate and the gas molecules.[40] The reason for the increase in work function of each system after gas adsorption is that the electronegativity of the doped metal is lower than that of O and F. This causes charge to tend to transfer from the metal atoms to the gas molecules,[50] which is consistent with the results of charge transfer.

3.3. Sensing Property Analysis. The adsorption properties of the three materials are investigated in a previous section. However, the sensing properties of the materials also need to be considered for their application. The sensing properties of gases mainly include sensitivity and recovery time.

From eqs 5 and 6, the sensitivity of the sensor is related to the band gap of the adsorption system. To obtain more accurate results, the HLE17 functional is used to calculate the band structure.[51,52] As shown in Figure 13, the band gaps of Pd-MoS_2, Pt-MoS_2, and Ni-MoS_2 before adsorption are 1.911, 1.815, and 1.722 eV, respectively. After adsorption, the band gaps are 1.551,

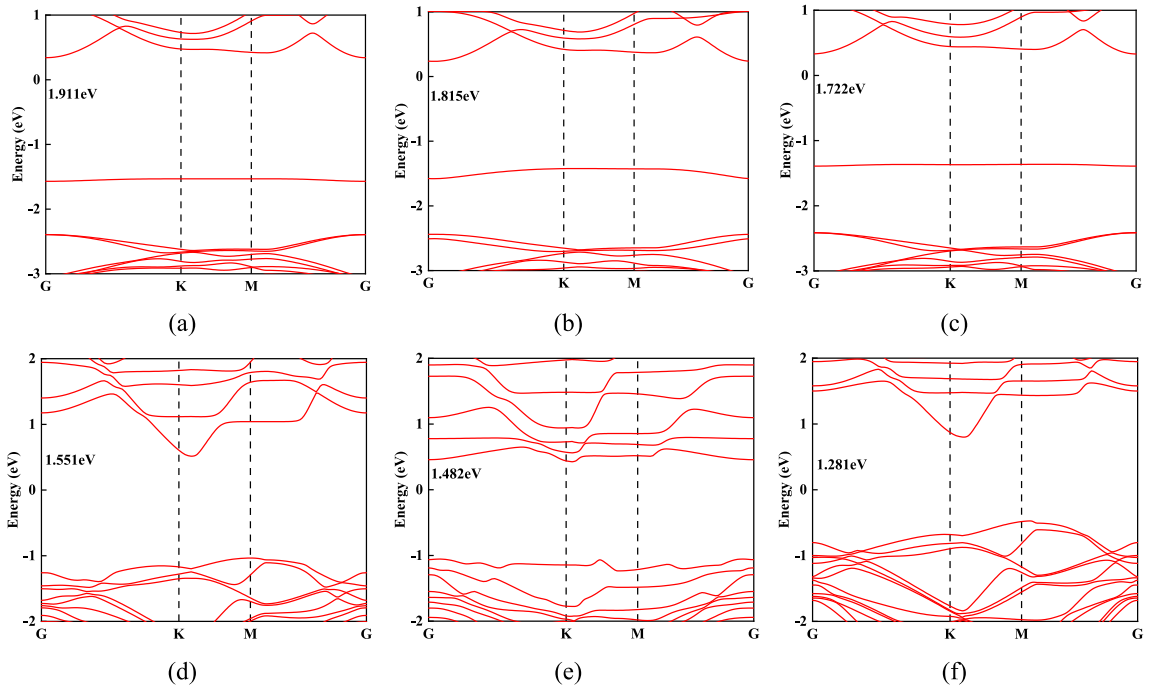

Figure 13. Band structure of (a) Pd-MoS_2, (b) Pt-MoS_2, (c) Ni-MoS_2, (d) $C_3H_2OF_6$/Pd-MoS_2, (e) $C_3H_2OF_6$/Pt-MoS_2, and (f) $C_3H_2OF_6$/Ni-MoS_2.

https://doi.org/10.1021/acsomega.4c05159
ACS Omega 2024, 9, 36659−36670

1.482, and 1.281 eV, in which Ni-MoS_2 exhibits the largest variation in band gap. The sensitivity of Pt-MoS_2 to $C_3H_2OF_6$ at 298, 348, and 398 K exceeds 99% (Figure 14).

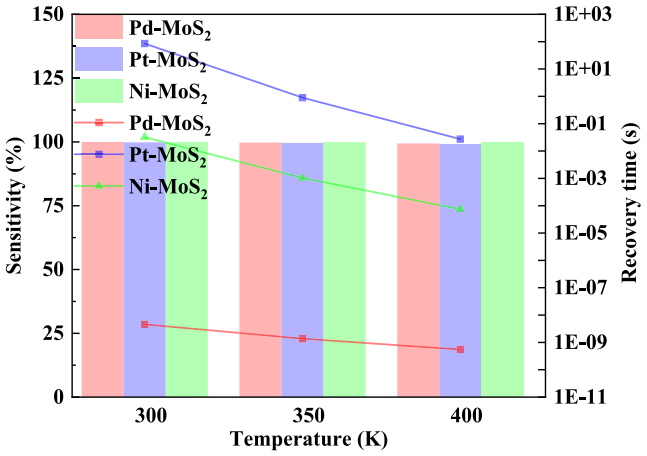

Figure 14. Sensitivity and recovery time of Pd-MoS_2, Pt-MoS_2 and Ni-MoS_2 to $C_3H_2OF_6$ under different temperature. The bar and dotted line graphs indicate sensitivity and recovery time, respectively.

The recovery time of the sensor can be calculated from eq 7. The recovery times of Pt-MoS_2 at 298, 348, and 398 K are 85.27, 0.89, and 0.027 s, respectively (Figure 10). Based on the results, the shorter recovery time is more desirable and indicates recyclability, making it promising as a $C_3H_2OF_6$ sensor. In contrast, Pd-MoS_2 and Ni-MoS_2 are not recommended for use as gas-sensitive materials in sensors due to their poor adsorption properties.

4. CONCLUSIONS

In this paper, the doping process of Pd, Pt, and Ni in MoS_2 is simulated based on first principles. The adsorption and sensing properties of Pd-MoS_2, Pt-MoS_2, and Ni-MoS_2 on $C_3H_2OF_6$ are also investigated. The doped structures are the most stable with the largest binding energy and electron transfer when the metal is doped at TMo. The adsorption energy and electron transfer of Pt-MoS_2 to $C_3H_2OF_6$ are the largest, reaching −0.834 eV and −0.235e, followed by Ni-MoS_2 and Pd-MoS_2. Meanwhile, the combined results of CDD, IGMH, ELF, and DOS calculations reveal a chemical bond forming between Pt-MoS_2 and $C_3H_2OF_6$, indicating chemisorption. The sensitivity and recovery time of Pt-MoS_2 meet the requirements of the sensor, suggesting the potential of Pt-MoS_2 for $C_3H_2OF_6$ gas sensors. Future experimental research can be conducted on the thermal stability and sensing response of samples.

■ ASSOCIATED CONTENT

Supporting Information

The Supporting Information is available free of charge at https://pubs.acs.org/doi/10.1021/acsomega.4c05159.

Brillouin zone meshing convergence and cutoff energy convergence test (PDF)

■ AUTHOR INFORMATION

Corresponding Author

Xiangdong Chen − *Department of Anesthesiology, Union Hospital, Tongji Medical College, Huazhong University of Science and Technology, Wuhan 430022, China; Institute of Anesthesia and Critical Care Medicine, Union Hospital, Tongji Medical College and Key Laboratory of Anesthesiology and Resuscitation, Ministry of Education, Huazhong University of Science and Technology, Wuhan 430022, China;* orcid.org/0000-0003-3347-2947; Email: xdchen@hust.edu.cn

Authors

Kaixin Wang − *Department of Anesthesiology, Union Hospital, Tongji Medical College, Huazhong University of Science and Technology, Wuhan 430022, China; Institute of Anesthesia and Critical Care Medicine, Union Hospital, Tongji Medical College and Key Laboratory of Anesthesiology and Resuscitation, Ministry of Education, Huazhong University of Science and Technology, Wuhan 430022, China*

Shiwen Fan − *Department of Anesthesiology, Union Hospital, Tongji Medical College, Huazhong University of Science and Technology, Wuhan 430022, China; Institute of Anesthesia and Critical Care Medicine, Union Hospital, Tongji Medical College and Key Laboratory of Anesthesiology and Resuscitation, Ministry of Education, Huazhong University of Science and Technology, Wuhan 430022, China*

Benli Liu − *Hubei Engineering Research Center for Safety Monitoring of New Energy and Power Grid Equipment, Hubei University of Technology, Wuhan 430068, China*

Weihao Liu − *Hubei Engineering Research Center for Safety Monitoring of New Energy and Power Grid Equipment, Hubei University of Technology, Wuhan 430068, China*

Complete contact information is available at: https://pubs.acs.org/10.1021/acsomega.4c05159

Author Contributions

⊥K.W. and S.F. contributed equally to this work and are the first authors.

Notes

The authors declare no competing financial interest.

■ ACKNOWLEDGMENTS

This work was supported by the National Key Research and Development Program of China (Grant 2018YFC2001802 to X.C.); National Natural Science Foundation (Grant 82071251 to X.C.); and Hubei Province Key Research and Development Program (Grant 2021BCA145 to X.C.).

■ REFERENCES

(1) Carron, M.; Tessari, I.; Linassi, F.; Navalesi, P. Desflurane versus propofol for general anesthesia maintenance in obese patients: A pilot meta-analysis. *J. Clin. Anesth.* **2021**, *68*, 110103.

(2) Gupta, A.; Stierer, T.; Zuckerman, R.; et al. Comparison of recovery profile after ambulatory anesthesia with propofol, isoflurane, sevoflurane and desflurane: a systematic review. *Anesth. Analg.* **2004**, *98* (3), 632−641.

(3) Larsen, B.; Seitz, A.; Larsen, R. Recovery of cognitive function after remifentanil-propofol anesthesia: a comparison with desflurane and sevoflurane anesthesia. *Anesth. Analg.* **2000**, *90* (1), 168−174.

(4) White, P. F.; Tang, J.; Wender, R. H.; et al. Desflurane versus sevoflurane for maintenance of outpatient anesthesia: the effect on early versus late recovery and perioperative coughing. *Anesth. Analg.* **2009**, *109* (2), 387−393.

(5) Kuo, H. C.; Hung, K. C.; Wang, H. Y.; et al. Prophylaxis for paediatric emergence delirium in desflurane-based anaesthesia: a network meta-analysis. *J. Anesth.* **2024**, *38* (2), 155−166.

(6) Jakobsson, J. Desflurane: A clinical update of a third-generation inhaled anaesthetic. *Acta Anaesthesiol. Scand.* **2012**, *56* (4), 420−432.

(7) Steffey, E. P.; Mama, K. R.; Brosnan, R. J.Inhalation Anesthetics. In *Veterinary Anesthesia and Analgesia: The Fifth Edition of Lumb and Jones*; Wiley, 2015; pp 297−331.
(8) Hu, E. P.; Yap, A.; Davies, J. F.; et al. Global practices in desflurane use. *Br. J. Anaesth.* **2023**, DOI: 10.1016/j.bja.2023.08.018.
(9) Dexter, F.; Hindman, B. J. Systematic review with meta-analysis of relative risk of prolonged times to tracheal extubation with desflurane versus sevoflurane or isoflurane. *J. Clin. Anesth.* **2023**, *90*, No. 111210.
(10) Nathanson, M. H.; Fredman, B.; Smith, I.; et al. Sevoflurane versus desflurane for outpatient anesthesia: a comparison of maintenance and recovery profiles. *Anesth. Analg.* **1995**, *81* (6), 1186−1190.
(11) Lei, L.; Ji, M.; Meng, Q.; Yang, J. J. Neurotoxicity of general anesthetics in the developing brain: Insight into the glutamate and GABA receptor signalling. *J. Anesth. Transl. Med.* **2022**, *1* (1), 10−19.
(12) He, Y.; Cheng, J.; Qin, H.; et al. Effects of Dexmedetomidine on Perioperative Brain Protection in Elderly Frail Patients. *J. Anesth. Transl. Med.* **2023**, *2* (3), 29−33.
(13) Pokhrel, L. R.; Grady, K. D. Risk assessment of occupational exposure to anesthesia Isoflurane in the hospital and veterinary settings. *Sci. Total Environ.* **2021**, *783*, No. 146894.
(14) Douglas, H. F.; Midon, M.; Floriano, D.; et al. Peri-anesthetic environmental and occupational exposure to desflurane waste anesthetic gas in a large animal veterinary hospital. *J. Occup. Environ. Med.* **2023**, *66*, 666−672.
(15) Han, F.; Zhao, J.; Zhao, G. Prolonged volatile anesthetic exposure exacerbates cognitive impairment and neuropathology in the 5xFAD mouse model of Alzheimer's disease. *J. Alzheimer's Dis.* **2021**, *84* (4), 1551−1562.
(16) Hooijmans, C. R.; Buijs, M.; Struijs, F.; et al. Exposure to halogenated ethers causes neurodegeneration and behavioural changes in young healthy experimental animals: a systematic review and meta analyses. *Sci. Rep.* **2023**, *13* (1), No. 8063.
(17) Wyssusek, K.; Chan, K. L.; Eames, G.; Whately, Y. Greenhouse gas reduction in anaesthesia practice: a departmental environmental strategy. *BMJ Open Qual.* **2022**, *11* (3), No. e001867.
(18) Gonzalez-Pizarro, P.; Muret, J.; Brazzi, L. The green anaesthesia dilemma: to which extent is it important to preserve as many drugs available as possible. *Curr. Opin. Anesthesiol.* **2023**, *36* (2), 196−201.
(19) Ryan, S. M.; Nielsen, C. J. Global warming potential of inhaled anesthetics: application to clinical use. *Anesth. Analg.* **2010**, *111* (1), 92−98.
(20) Laskar, M. R.; Nath, D. N.; Ma, L.; et al. p-type doping of MoS2 thin films using Nb. *Appl. Phys. Lett.* **2014**, *104* (9), No. 092104, DOI: 10.1063/1.4867197.
(21) McGinn, C. K.; Lamport, Z. A.; Kymissis, I. Review of gravimetric sensing of volatile organic compounds. *ACS Sens.* **2020**, *5* (6), 1514−1534.
(22) Allsop, T.; Neal, R. A review: Application and implementation of optic fibre sensors for gas detection. *Sensors* **2021**, *21* (20), 6755.
(23) Jin, C.; Rasmussen, F. A.; Thygesen, K. S. Tuning the Schottky barrier at the graphene/MoS2 interface by electron doping: density functional theory and many-body calculations. *J. Phys. Chem. C* **2015**, *119* (34), 19928−19933.
(24) McClellan, C. J.; Yalon, E.; Smithe, K. K. H.; et al. High current density in monolayer MoS2 doped by AlOx. *ACS Nano* **2021**, *15* (1), 1587−1596.
(25) Piosik, E.; Szary, M. J. Development of MoS2 doping strategy for enhanced SO2 detection at room temperature. *Appl. Surf. Sci.* **2023**, *638*, No. 158013.
(26) Mia, A. K.; Meyyappan, M.; Giri, P. K. Two-dimensional transition metal dichalcogenide based biosensors: from fundamentals to healthcare applications. *Biosensors* **2023**, *13* (2), 169.
(27) Lakshmy, S.; Kundu, A.; Kalarikkal, N.; et al. Pd-functionalized 2D TMDC $MoTe_2$ monolayer as an efficient glucose Sensor: A First-principles DFT study. *Appl. Surf. Sci.* **2023**, *631*, No. 157525.
(28) Wan, Q.; Chen, X.; Xiao, S. Ru-Doped $PtTe_2$ Monolayer as a Promising Exhaled Breath Sensor for Early Diagnosis of Lung Cancer: A First-Principles Study. *Chemosensors* **2022**, *10* (10), 428.
(29) Sadeghi, M.; Jahanshahi, M. Design of Biosensors Based Transition-Metal Dichalcogenide for DNA-base Detection: A First-Principles Density Functional Theory Study. *Nanochem. Res.* **2019**, *4* (1), 27−34.
(30) Lembke, D.; Bertolazzi, S.; Kis, A. Single-layer MoS2 electronics. *Acc. Chem. Res.* **2015**, *48* (1), 100−110.
(31) Luo, H.; Cao, Y.; Zhou, J.; et al. Adsorption of NO2, NH3 on monolayer MoS2 doped with Al, Si, and P: A first-principles study. *Chem. Phys. Lett.* **2016**, *643*, 27−33.
(32) Szary, M. J. MoS2 doping for enhanced H2S detection. *Appl. Surf. Sci.* **2021**, *547*, No. 149026.
(33) Li, B.; Zhou, Q.; Peng, R.; et al. Adsorption of SF6 decomposition gases (H2S, SO2, SOF2 and SO2F2) on Sc-doped MoS2 surface: A DFT study. *Appl. Surf. Sci.* **2021**, *549*, No. 149271.
(34) Zhang, R.; Fu, D.; Ni, J.; et al. Adsorption for SO2 gas molecules on B, N, P and Al doped MoS2: The DFT study. *Chem. Phys. Lett.* **2019**, *715*, 273−277.
(35) VandeVondele, J.; Krack, M.; Mohamed, F.; et al. Quickstep: Fast and accurate density functional calculations using a mixed Gaussian and plane waves approach. *Comput. Phys. Commun.* **2005**, *167* (2), 103−128.
(36) Grimme, S.; Ehrlich, S.; Goerigk, L. Effect of the damping function in dispersion corrected density functional theory. *J. Comput. Chem.* **2011**, *32* (7), 1456−1465.
(37) Marom, N.; Tkatchenko, A.; Rossi, M.; et al. Dispersion interactions with density-functional theory: Benchmarking semi-empirical and interatomic pairwise corrected density functionals. *J. Chem. Theory Comput.* **2011**, *7* (12), 3944−3951.
(38) Grimme, S.; Antony, J.; Ehrlich, S.; Krieg, H. A consistent and accurate ab initio parametrization of density functional dispersion correction (DFT-D) for the 94 elements H-Pu. *J. Chem. Phys.* **2010**, *132* (15), No. 154104, DOI: 10.1063/1.3382344.
(39) Lu, T.; Chen, Q. Independent gradient model based on Hirshfeld partition: A new method for visual study of interactions in chemical systems. *J. Comput. Chem.* **2022**, *43* (8), 539−555.
(40) Lefebvre, C.; Rubez, G.; Khartabil, H.; et al. Accurately extracting the signature of intermolecular interactions present in the NCI plot of the reduced density gradient versus electron density. *Phys. Chem. Chem. Phys.* **2017**, *19* (27), 17928−17936.
(41) Burdett, J. K.; McCormick, T. A. Electron localization in molecules and solids: the meaning of ELF. *J. Phys. Chem. A* **1998**, *102* (31), 6366−6372.
(42) Lu, T.; Chen, Q. Revealing molecular electronic structure via analysis of valence electron density. *Acta Physicochim. Sin.* **2018**, *34* (5), 503−513.
(43) Lu, T.; Chen, F. Multiwfn: A multifunctional wavefunction analyzer. *J. Comput. Chem.* **2012**, *33* (5), 580−592.
(44) Poornimadevi, C.; Kala, C. P.; Thiruvadigal, D. J. First principle analysis of toxic gas adsorption on pristine WS_2 and Fe-doped WS_2: Implications for gas sensing. *Surf. Interfaces* **2023**, *42*, No. 103518.
(45) Togo, A.; Chaput, L.; Tadano, T.; Tanaka, I. Implementation strategies in phonopy and phono3py. *J. Phys.: Condens. Matter* **2023**, *35* (35), No. 353001.
(46) Bott, G.; Field, L. D.; Sternhell, S. Steric effects. A study of a rationally designed system. *J. Am. Chem. Soc.* **1980**, *102* (17), 5618−5626.
(47) Chen, L.; Wang, X.; Shi, S.; et al. Tuning the work function of VO_2 (1 0 0) surface by Ag adsorption and incorporation: Insights from first-principles calculations. *Appl. Surf. Sci.* **2016**, *367*, 507−517.
(48) De Leeuw, N. H.; Purton, J. A.; Parker, S. C.; et al. Density functional theory calculations of adsorption of water at calcium oxide and calcium fluoride surfaces. *Surf. Sci.* **2000**, *452* (1−3), 9−19.
(49) Jiang, Q.; Zhang, J.; Ao, Z.; et al. First principles study on the CO oxidation on Mn-embedded divacancy graphene. *Front. Chem.* **2018**, *6*, 187.
(50) Li, L.; Song, L.; Zhang, X.; et al. Effect of substitutional and interstitial boron-doped $NiCo_2S_4$ on the electronic structure and surface adsorption: high rate and long-term stability. *ACS Appl. Energy Mater.* **2022**, *5* (2), 2505−2513.

(51) Verma, P.; Truhlar, D. G. HLE17: An improved local exchange−correlation functional for computing semiconductor band gaps and molecular excitation energies. *J. Phys. Chem. C* **2017**, *121* (13), 7144−7154.
(52) Choudhuri, I.; Truhlar, D. G. HLE17: An efficient way to predict band gaps of complex materials. *J. Phys. Chem. C* **2019**, *123* (28), 17416−17424.

https://doi.org/10.1021/acsomega.4c05159
ACS Omega 2024, 9, 36659−36670